Preparation of BiOCl from industrial waste salt and its photocatalytic performance

Jukui Gao[1], Wei Chang[1]*, Zhiyuan Ren[1], Peiqi Yao[1], Bin Liu[1], Yunfen Li[1]*

[1]*Xi'an Key Laboratory of Textile Chemical Engineering Auxiliaries, School of Environmental and Chemical Engineering, Xi'an Polytechnic University, Xi'an, China.*

ABSTRACT

This study synthesized a high-performance BiOCl using a straightforward and efficient hydrolysis process, leveraging chlorine-containing industrial waste salt (IWS) as the primary raw material. The characterization of the as-materials was assessed using SEM, XRD, PL, XPS, UV-Vis DRS, EIS, etc. The BiOCl (GB) derived from IWS exhibited a significant number of oxygen vacancies, substantial exposure of (010) facets, an enlarged surface area, and enhanced absorption of visible light. Photocatalytic experiments revealed that GB could achieve a 92.8% degradation rate of rhodamine B(RhB) under 60 min of illumination, outperforming BiOCl synthesized from NaCl. These results suggest that hydrolysis method is a simple and effective but promising IWS preconditioning and resource utilization strategy.

KEYWORDS

BiOCl, Hydrolysis method, Photocatalysis, Industrial waste salt

Received 9 December 2024, revised 12 December 2024, accepted 5 March 2025

INTRODUCTION

Industrial waste salt (IWS) is produced in large quantities by the chemical, pharmaceutical, and other industries.[1] Its composition is complex, derived from a variety of sources, and contains a wide range of hazardous and toxic substances.[2] It also has high treatment costs and is classified as industrial waste in the waste solid. The recent increase in IWS production in China is estimated to surpass 20 million tons annually and will increase consecutively.[3] Hence, disposing of IWS safely and effectively has become a critical environmental and developmental issue in China. IWS typically contains significant amounts of organic and inorganic pollutants in addition to NaCl and Na_2SO_4.[4] Under these circumstances, how to recycle useful resources and detoxify IWS is a dilemma that must not be neglected for not only company development but environmental protection.[5] Currently, the treatment of IWS is mainly landfills and sea discharge, however, their limitations are also disappointing. Landfills are simple and low-cost, but they occupy a vast area and are heavily polluting while sea discharge is mainly suitable for offshore areas and cannot be dispensed across the entire nation.[6] Considering the peculiarity and puzzle in the treatment of IWS, researchers are diligently exploring the valuable resource utilization of IWS and have made great strides. As an essential component of IWS, chlorides like NaCl represent the next generation of molten salts with significant development potential. Xi et al. used pyrolysis to remove pollutants from the waste salts, [5] producing molten salts that can be used for solar power generation, thermal energy storage, and other applications.[7] Chlorine-containing waste salt can also be used in the chlor-alkali industry. IWS recycling can be achieved through the application of the chlor-alkali membrane electrolyze method.[2] Yao et al. successfully prepared high-performance BiOCl using chlorine-containing wastewater, providing new insights into the utilization of waste salts in catalyst preparation.[8]

Bismuth oxychloride (BiOCl) is a typical V-VI-VII ternary oxide with low toxicity, stable chemical properties, and an easily adjustable electronic energy band structure.[9] The crystalline form of BiOCl belongs to the tetragonal structure of n-PbFCl (PbFCl) type, which consists of alternating Cl^- and $[Bi_2O_2]^{2+}$ layers, with a wide forbidden bandwidth (3.19 eV-3.60 eV), which is favorable for the reduction of photogenerated carrier combination rate, and the disadvantage is the low utilization rate of the sunlight (about 4%).[10-12] In the field of photocatalysis, moreover, BiOCl presents other advantages, such as effective electron transport, outstanding photocatalytic capabilities, and a simple synthesis process, establishing it as a prominent option in the realm of bismuth-based photocatalysts.[13] The catalyst's crystalline form has a significant impact on its performance. Different crystalline surfaces of single-crystal materials have different geometrical and electronic structures, which endow them with different properties and edges.[14-16] The (001) facet of BiOCl exhibits higher activity during photocatalysis due to its perpendicularity to the built-in electric field, a high concentration of hydrogen ions can control its growth, whereas the (010) crystalline facet is an open-channel structure and exposes both ligand-unsaturated Bi, O, and Cl atoms, which can be used to promote the growth by a neutral environment.[17-20] Other modification methods, such as introducing oxygen vacancies can provide new and more reliable reactant adsorption sites and influence the electronic structure of adsorbates, thus enhancing the photovoltaic properties of materials.[21,22]

Based on the IWS samples we received from enterprises, we found that its composition is mostly non-metallic elements and contains a large amount of chlorine, so we explored the feasibility of using it as a raw material for the preparation of BiOCl with excellent performance, to provide a reference basis for the resource utilization of those IWS. Given the cost and scale limitations associated with the treatment process, the hydrothermal method is deemed unsatisfactory due to its high expenses and potential inefficiencies at larger scales. Consequently, the hydrolysis method has been chosen as the preferred approach.

MATERIALS AND METHODS

Reagents and instrumentation

Sodium chloride (NaCl), bismuth nitrate pentahydrate ($Bi(NO_3)_3{\cdot}5H_2O$), anhydrous ethanol (C_2H_5OH), sodium hydroxide (NaOH), rhodamine B (RhB), deionized water. All chemicals used in this study are analytical grade and without further purification.

The IWS samples used in this experiment were from petrochemical enterprises in Gansu, Yulin, and Shanbei in China, labeled as GF, YF, and SF respectively, and their elemental composition is given in Table 1.

X-ray diffractometer (Mini Flex 600, Rigaku, Japan), field emission scanning electron microscope (JEOL JSM 6700F, FEI), UV-visible

*To whom correspondence should be addressed
Email: changwei72@163.com

ISSN 1996-840X Online / South African Chemical Institute / http://saci.co.za/journal

https://doi.org/10.17159/0379-4350/2025/v79a03

Table 1: The composition of waste salt

Sample	Elements（×10³ ppm）									
	Al	Si	S	K	Ca	Fe	Na	Br	Cu	Cl
GF	-	1.345	0.0817	-	-	0.006	40.85	0.009	0.0509	164.7
YF	-	0.8613	32.11	0.4256	-	-	-	0.0385	0.03	43.79
SF	21.99	48.31	692.7	10.19	22.85	0.4921	-	1.581	0.5504	199.3

- Undetected

diffuse reflectance spectrometer (U-3310, Hitachi, Japan), and electrochemical workstation (VSP-300, Bioroger, France) were used for material characterization. The surface chemical elements of the sample were detected by X-ray photoelectron spectroscopy (ULVAC-PHI, PHI5000 Versa Probe III).

Catalysts Preparation

In a typical synthesis, 3 mmol of Bi $(NO_3)_3{\cdot}5H_2O$ and 3 mmol of NaCl were added to 40 mL distilled water at room temperature with continuous stirring for 120 min, and 6 mol/L NaOH solution was added to this mixture to adjust its pH to 1. The sample obtained was labeled as NB. Other BiOCl samples were prepared according to the above procedure using GF, YF, and SF, each containing 3 mmol of Cl^-, as the chlorine sources. These samples were named GB, YB, and SB, respectively.

Photodegradation Evaluation

The as-prepared sample (10 mg) was added into 20 mL (10 mg/L) of RhB solution. The photocatalytic reaction was implemented in a photochemical reactor (XPA, Nanjing Xujiang Electromechanical Factory, Nanjing, China). After a dark reaction for 30 min to reach the adsorption-desorption equilibrium, the light source (500W xenon lamp) was granted for photocatalytic experiments. The supernatant was taken at given time intervals (15 min), and the absorbance was measured at 554 nm using a UV spectrophotometer (UV-2450, Shimadzu Co., Ltd., Japan) and calculated according to the following equation (1):

$$\Phi\ (\%) = (c/c_0) \times 100 \quad (1)$$

where Φ, c and c_0 are the RhB removal rate, the concentration at different reaction time and the initial concentration of RhB solution, respectively.

RESULTS AND DISCUSSION

SEM Analysis

Figure 1 shows the SEM image of the prepared samples. It can be observed that the prepared BiOCl is mostly in the form of clusters, but there are some differences due to different chlorine sources of the IWS. While NB (Figure 1a) exhibits flaky and clustered morphology, there is a greater degree of aggregation phenomena and inadequate dispersion. The majority of GB (Figure 1b) is distributed more evenly and in the shape of clusters. YB (Figure 1c) mostly consists of flakes and scattered clusters, there is not much evidence of a significant agglomeration process. SB (Figure 1d) exhibits the most severe clustering and aggregation phenomenon, with significant variability in particle diameter. This crystal appearance might be due to the participation of other components in the SF that inhibit the formation of crystals.

XRD Analysis

The prepared sample's XRD pattern is displayed in Figure 2. Notably, all the samples that were obtained exhibit clear characteristic peaks at 11.98°, 24.13°, 25.84°, 32.49°, 33.44°, 40.89°, 46.63°, and 49.69°. These peaks are consistent with the standard peaks of BiOCl (PDF#99-000-0389) and correspond to the 001, 002, 101, 110, 102, 200, and 113 crystal facets. The diffraction peaks of SB (Figure 2) are lower and broader, suggesting that the crystallinity of SB is poorer than that of the other samples. The 001 diffraction peak of GB is significantly weaker than that of NB, and the rest of the diffraction peaks are also weakened. The literature reports that hydrothermal or solvent-thermal techniques can be utilized to prepare BiOCl with varying facet exposures.[22-24] The fact that the ratio of the 002 to 200 peak intensities is less than 1 further suggests that the 010 facet of all the prepared samples is exposed.[9,14,25]

XPS Analysis

XPS spectra of NB and GB were analyzed to understand whether the BiOCl produced from the IWS has differences in composition and chemical valence states of the surface elements. As shown in Figure 3a, the peaks of Bi 4f at 159.3 eV and 164.6 eV correspond to Bi 4f 7/2 and Bi 4f 5/2, respectively, suggesting that the element Bi is ortho-3-valent in GB.[26,27] Figure 3b shows the XPS spectra of Cl 2p XPS spectra, with the main peak at 197.8 eV attributed to Cl 2p 3/2 and the peak at 199.5 eV attributed to Cl 2p 1/2.[15,16] As shown in Figure 3c and Figure 3d, the peaks with the binding energy of 529.9 eV, 533.1 eV, and 531.5 eV correspond to lattice oxygen of Bi-O, the chemisorbed H_2O (-OH) on the surface of photocatalyst and OVs, respectively.[28,29] The lattice oxygen content on the GB sample decreases while the content of OVs increases.

From the survey XPS profile in Figure 3e, the GB and NB are identical, indicating no significant difference in the composition of the elements. By calculation, the contents of Bi, O, and Cl in NB are 27.94%, 43.05%, and 29.01%, respectively, while in GB, the contents are 28.65%, 40.73%, and 30.62%, respectively. There is a noticeable difference in the oxygen content between the two samples, and it further indicates that the GB contains a higher number of oxygen vacancies, which can accelerate the electron transfer or speed up the reaction by adsorption of oxygen molecules during the photocatalytic process. The presence of oxygen vacancies does not affect the crystalline structure of BiOCl but weakens the intensity of the diffraction peak of the 001 facet, which is consistent with the XRD result.[30] Furthermore, the GB is a pale yellow powder, consistent with the color description of defective samples with oxygen vacancies in the literature.[31]

Specific Surface Area

Specific surface area is an important parameter for evaluating photocatalytic active sites of material. In general, the larger the specific surface area the better the photocatalytic performance because of the additional photocatalytic active sites.[32] The nitrogen adsorption-desorption curves of GB and NB are shown in Figure 4, and the specific surface area of GB is 14.98 m^2/g, which is 1.5 times that of NB. The detailed data of GB and NB are shown in Table 2. The surface area of BiOCl exposed on the 010 crystal plane is larger than that exposed on the 001 crystal plane, which also corroborates the fact that GB is the 010 plane exposure.[33,34]

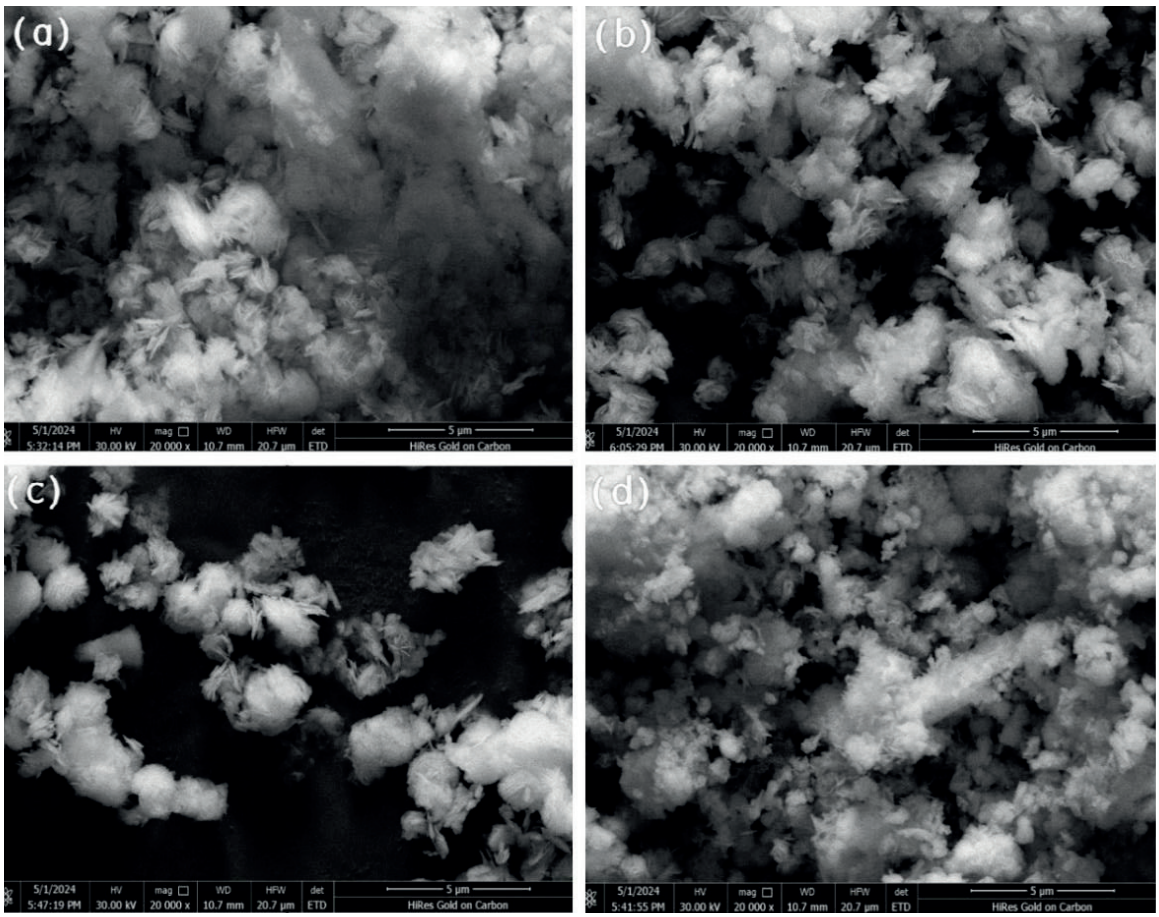

Figure 1: SEM image of the prepared samples (a) NB, (b) GB, (c) YB, (d) SB

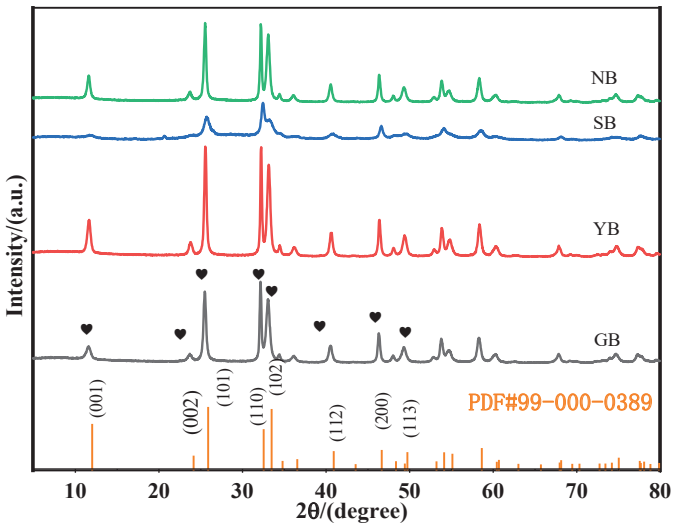

Figure 2: XRD patterns of the prepared samples

Photoelectric Properties

Figure 5a shows the UV-Vis diffuse reflectance spectroscopy of the prepared samples. It is clear that both GB and YB exhibit significant absorption in the visible light range. The band gap (Eg) is calculated according to the Kubelka-Munk function (Equation 2):

$$\alpha h\eta = A(h\eta - Eg)^{n/2} \quad (2)$$

where α is the absorption coefficient (L/(g*cm)), h is the Planck constant (6.626×10^{-34} J·s), A is the absorptivity, η is the optical frequency (Hz), Eg is the bandgap(eV), n value for semiconductors is set to 1 for those with a general direct bandgap, and 4 for those with an indirect bandgap.[26]

As shown in Figure 5b, the bandgap of GB and YB were calculated and plotted to be 3.06 eV, while the bandgap of SB and NB were 3.29 eV and 3.19 eV respectively. It is easy to see that GB showed the best performance in terms of absorption in the visible region. The visible light absorption of the YB is also slightly stronger than that of the NB. The visible absorption ranges of GB and YB were enhanced by elemental doping or the introduction of oxygen vacancies.[30,31] Given that no other elements were detected in EDS and XPS, the enhanced light absorption of GB and YB comes from oxygen vacancies, which is consistent with the XPS elemental analysis.[35-38]

Fluorescence analysis (PL) is used to measure the photogenerated carrier combination rate of photocatalysts using the principle of photoluminescence.[39] The lower the fluorescence intensity, the slower the photogenerated carrier combination rate of the photocatalyst and the better photocatalytic performance.[40,41] As shown in Figure 6, except for the YB, the fluorescence intensities of GB and SB were lower than those of NB, with GB exhibiting the lowest intensity. This suggests that the recombination of photogenerated carriers is suppressed, potentially enhancing its photocatalytic activity.

Electrochemical Impedance Analysis

Electrochemical impedance spectroscopy (EIS) can be used to study the interfacial charge transfer capability of a material by plotting a Nyquist diagram to characterize the magnitude of the charge transfer resistance, with a smaller arc radius representing a lower resistance and a higher efficiency of its photogenerated carrier separation.[27,35] The EIS test results for GB, YB, and NB are depicted in Figure 7. The NB sample exhibits the largest arc radius. In contrast, GB has the smallest, indicating that GB possesses a high efficiency in separating

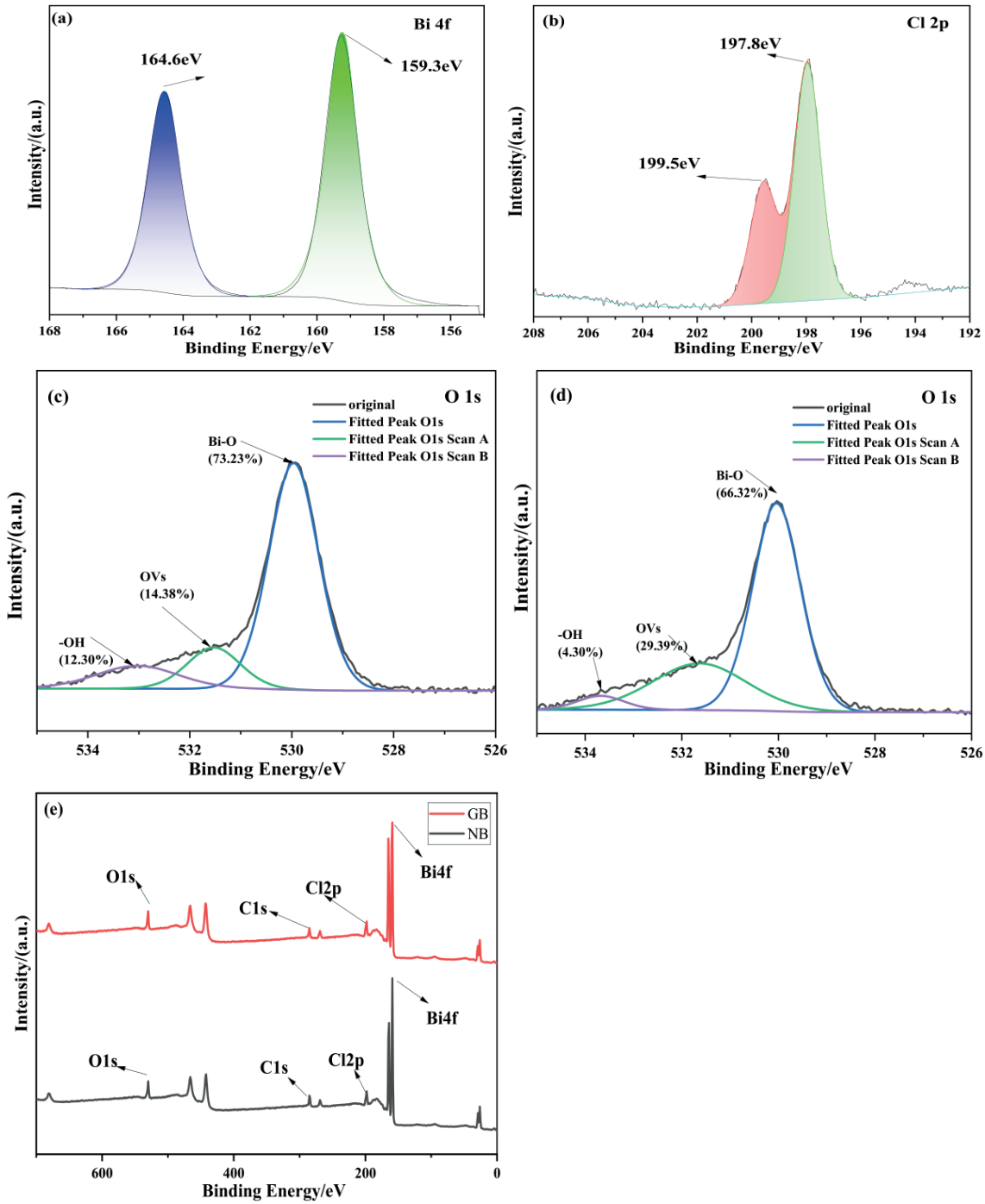

Figure 3: (a) Bi 4f, (b) Cl 2p spectra of GB, (c) O1 s of NB, (d) O1 s of GB, (e) XPS survey spectra of GB and NB

photogenerated carriers and exhibits the highest photocatalytic activity. This finding is consistent with the results obtained from fluorescence analysis.

Mott-Schottky analysis

To further explore the valence band (VB) and conduction band (CB) potentials of the samples, Mott-Schottky (M-S) tests were performed. Figure 8(a-c) shows the M-S curves of NB, GB, and YB, respectively. The intersection of the tangent lines of the curves with the X-axis gives the values of their conduction band (CB) potentials, which are -0.43 V, -0.51 V, and -0.45 V, respectively. The more negative the value of CB is, the more the material has a strong reducing ability. According to the equation (3), the conduction band values of each sample can be calculated. The results are shown in Table 3.

$$E_{VB} = E_{CB} + Eg \quad (3)$$

where E_{VB} is the valence band potential (V), E_{CB} is the conduction band potential (V) obtained from Figure 8, and the Eg is the band gap energy (eV) obtained from Figure 5(b).

Photocatalytic Activity

Figure 9a shows the results of photocatalytic degradation of RhB for the prepared samples. It is evident that GB demonstrates the most effective photocatalytic activity, degrading 92.8% of RhB within 60 min. YB follows this with 86.4% degradation, and NB with 83.7%. In contrast, SB performs poorly, with only 50.2% degradation. The kinetic curve was fitted according to the first-order kinetic model equation (4), The results are shown in Figure 9(b). It is easy to observe that GB has the largest rate constant of 0.02613 min^{-1} (the slope of graph in Figure 9(b)), and SB has the smallest rate constant of 0.00731 min^{-1}, indicating better photocatalytic activity of GB. In

conclusion, the exposure of the (010) facet, preferable crystallinity, an increased specific surface area, superior light absorption, enhanced photovoltaic properties, and a greater number of oxygen vacancies, make GB the most effective for the degradation of RhB.

$$\ln(C_0/C) = kt \quad (4)$$

where C_0 and C are the concentrations of RhB at time t = 0 and t = t, respectively, and k is the first-order rate constant.

To further investigate the reuse performance and photocatalytic stability of the material, photocatalytic cycling experiments were conducted using GB. The GB was cleaned and recycled by soaking it with ethanol for 3 h at the end of each cycle. As shown in Figure 10, the degradation of RhB by GB was still 87.5% after three cycles, which indicates that GB has better photocatalytic stability and recyclability.

Table 2: Specific surface area and pore size analysis results

Sample	Surface area(m^2/g)	Pore volume(cm^3/g)	Pore size (nm)
GB	14.98	0.2479	55.56
NB	10.30	0.1705	55.81

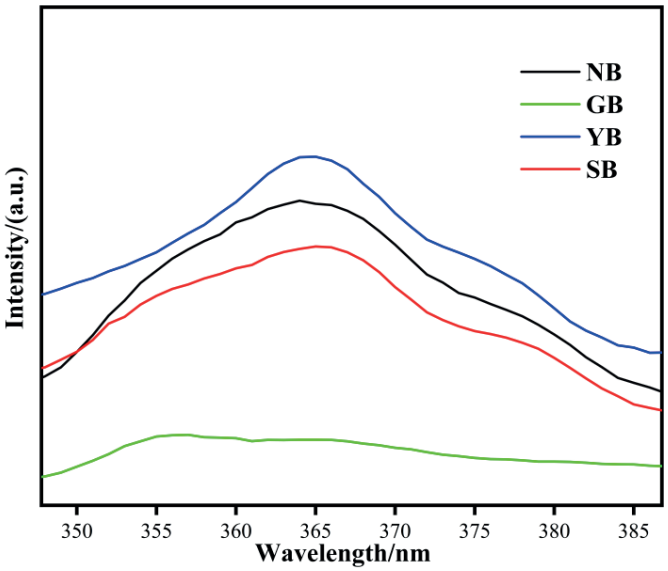

Figure 6: PL spectra of the prepared samples

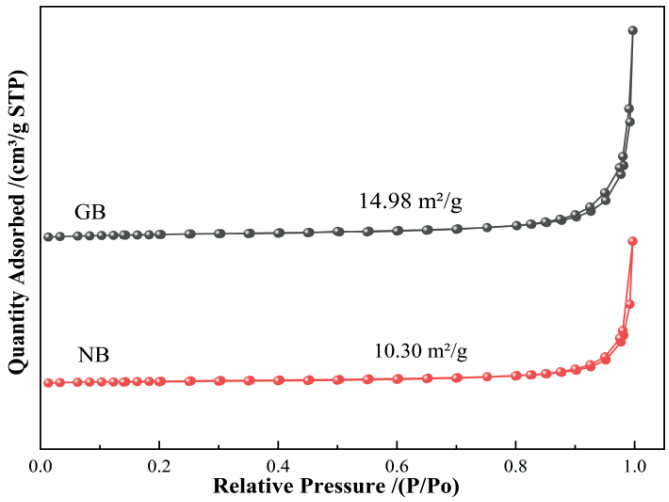

Figure 4: N_2 adsorption-desorption isotherm of the GB and NB

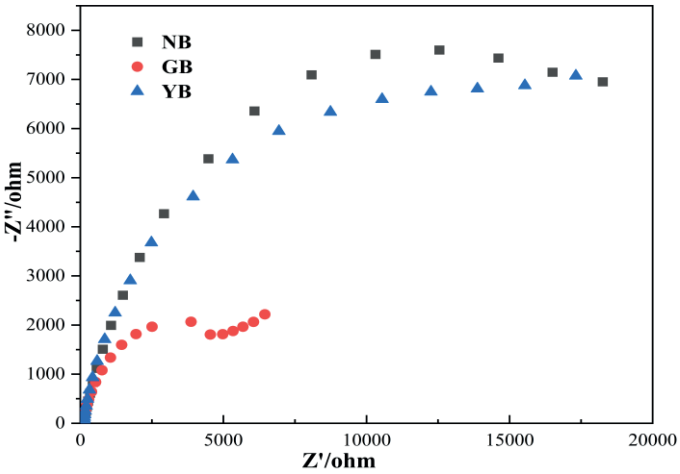

Figure 7: Electrochemical impedance spectra of the prepared samples

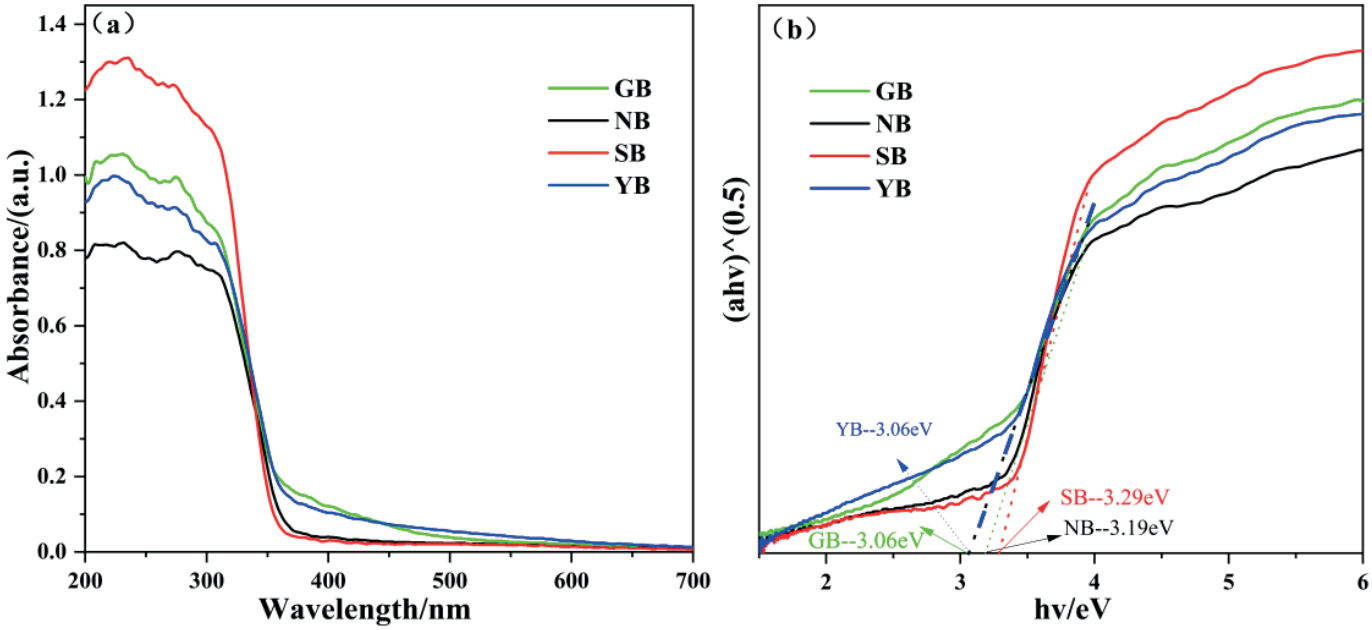

Figure 5: (a) UV-Visible diffuse reflection spectra and (b) band gap spectra of the prepared samples

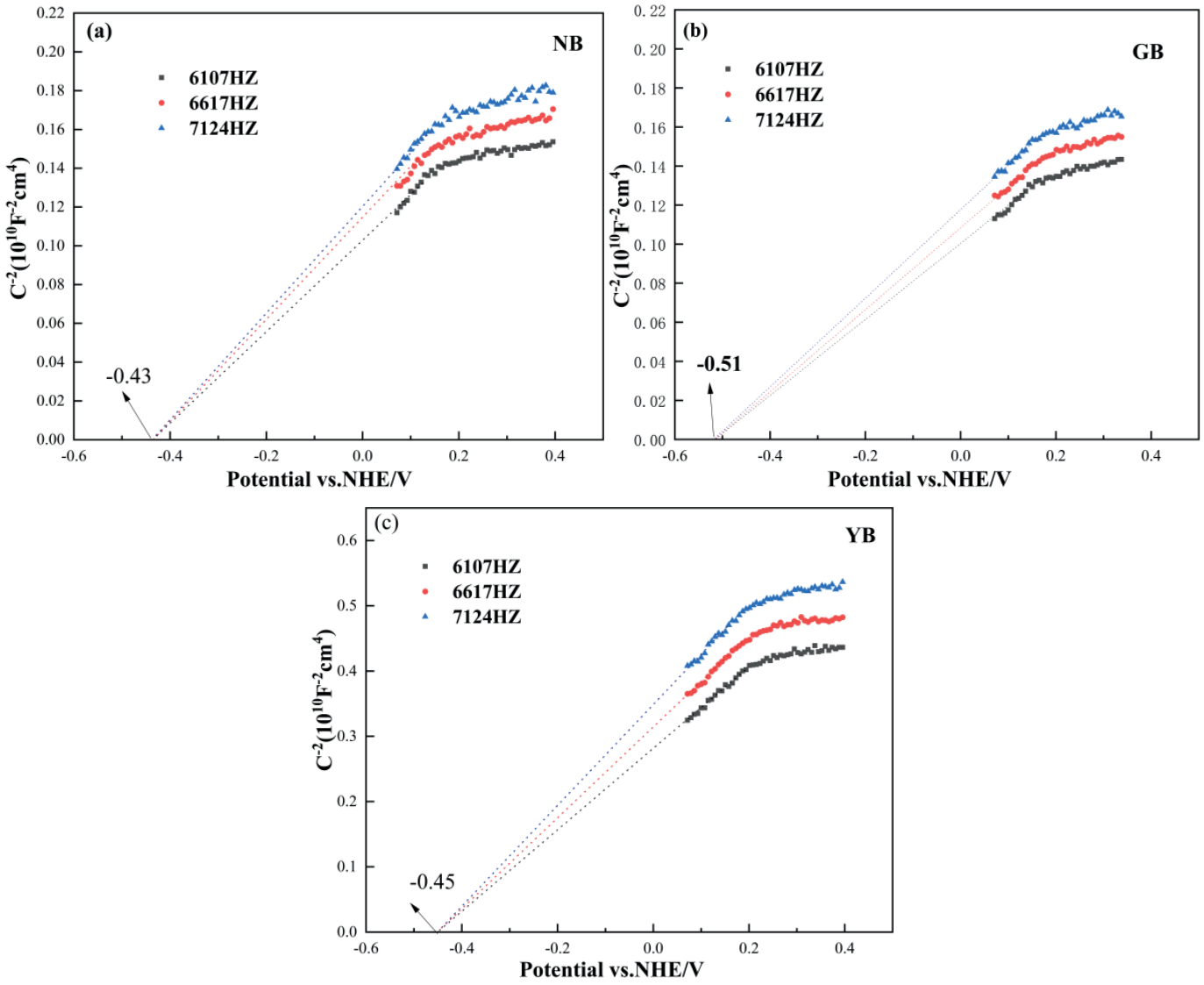

Figure 8: Mott-Schottky plots for (a) NB, (b) GB, (c) YB

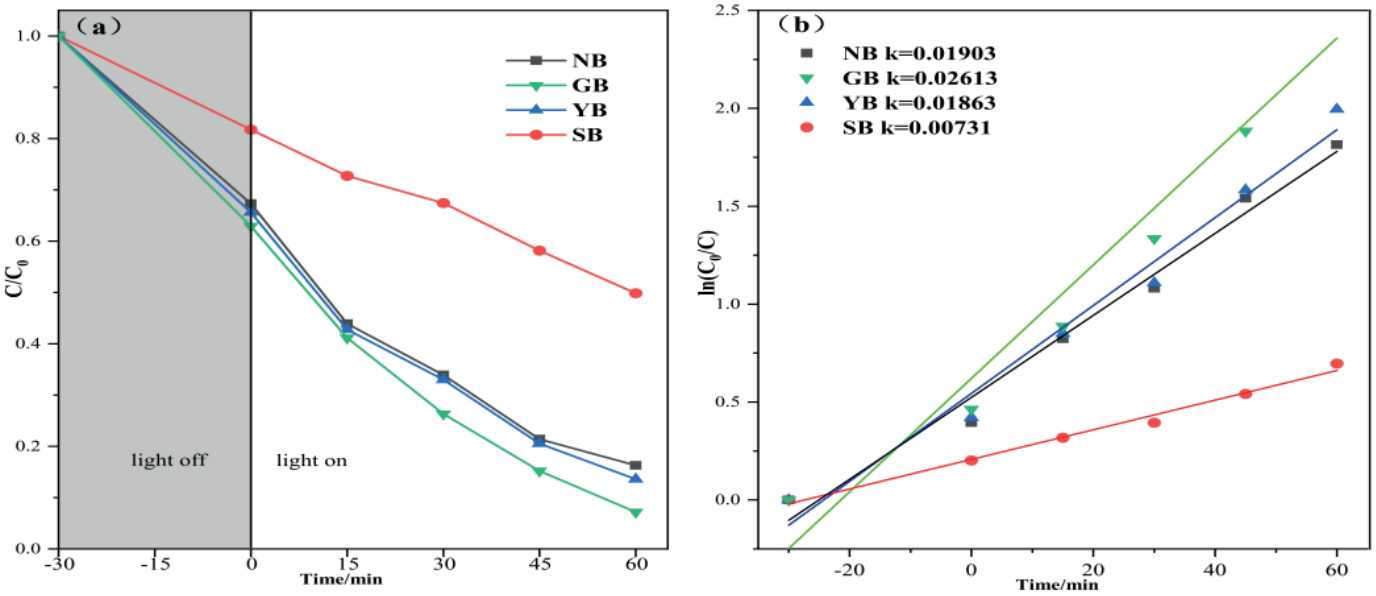

Figure 9: (a) Photocatalytic performance diagram (b) First-order kinetics curve of different samples

Table 3: Energy band statistics of the prepared samples

Sample	NB	GB	YB
E_{VB}	2.76 V	2.55 V	2.84 V
E_{CB}	-0.43 V	-0.51 V	-0.45 V
Eg	3.19 eV	3.06 eV	3.06 eV

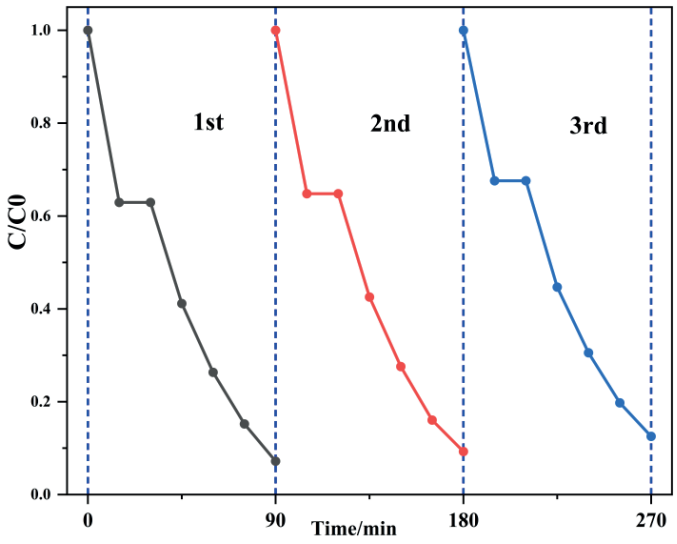

Figure 10: Cyclic degradation of RhB by GB

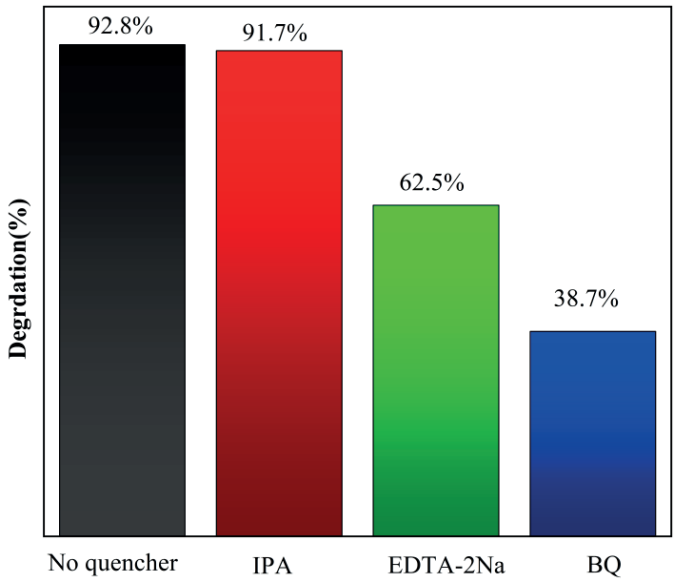

Figure 11: RhB's degradation rate with different trapping agents

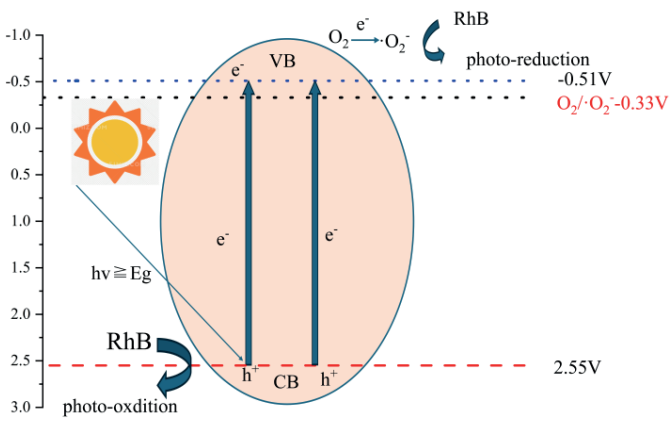

Figure 12: Schematic mechanism of the photocatalytic degradation of GB

Photocatalytic Mechanism

To investigate the photocatalytic mechanism, the radical trapping experiment was taken. The isopropanol (IPA), disodium ethylenediaminetetraacetic acid (EDTA), and p-benzoquinone (BQ) were used during the photocatalytic process to capture •OH, h^+, and $\bullet O_2^-$, respectively. The results are shown in Figure 11. The degradation rate of RhB by the GB reached 92.8% within 60 min without the addition of any trapping agent. The rate remained relatively stable at 91.7% after the introduction of IPA. However, upon the addition of EDTA, the degradation rate decreased to 62.5%, suggesting that h^+ plays a significant role in the RhB degradation process. Further, the degradation rate fell to 38.7% with the addition of BQ, indicating that $\bullet O_2^-$ is the primary active species involved in RhB degradation. Consequently, it can be inferred that •OH is minimally involved in the RhB degradation during the photocatalytic process, while $\bullet O_2^-$ and h^+ are the predominant and secondary active species, respectively.

The proposed photocatalytic mechanism is illustrated in Figure 12. Upon light irradiation of BiOCl, photogenerated carriers are produced, where e^- from the valence band are excited to the conduction band and react with O_2 in the solution to form superoxide radicals $\bullet O_2^-$ (-0.33 V). These radicals then interact with RhB; concurrently, the h^+ in the valence band also engages in reactions with RhB, thereby achieving the high efficiency of pollutant degradation. The oxygen vacancies on the 001 facet can generate superoxide radicals $\bullet O_2^-$ through single-electron reduction; meanwhile, the 010 facet can adsorb water molecules in a dissociated state, which facilitates the capture of h^+ both thermodynamically and kinetically.[21,31,33] These suggest that the degradation of RhB is facilitated by the synergistic action of the 001) and 010 facets during the photocatalytic process. Furthermore, the presence of oxygen vacancies enhances GB's photocatalytic activity.

CONCLUSIONS

In this paper, BiOCl was prepared by hydrolysis method using industrial waste salt as raw material. Different IWS have effects on the morphology, crystal shape, specific surface area, and optical properties of the prepared BiOCl due to their compositional differences. In this experiment, the BiOCl prepared from GF has the best photocatalytic activity, which is related to its higher crystallinity, larger specific surface area, considerable number of oxygen vacancies with lower bandgap energy, excellent visible light absorption, and efficient carrier separation efficiency.

The experimental findings reported in this paper also demonstrate that the elemental species present in IWS significantly impact the synthesis of the sample, a factor closely tied to the intricate composition of the IWS. Furthermore, the presence of excess sulfur may account for the reduced crystallinity and suboptimal photocatalytic performance observed in SB. The coexistence of various elements in IWS can facilitate the formation of oxygen vacancies or induce elemental doping in BiOCl, suggesting that GF and YF can be utilized to synthesize BiOCl when their composition is maintained at a relatively stable level. Even for SB, which exhibits relatively poor activity, there is a noticeable enhancement in photovoltaic properties, indicating that it holds potential for practical applications. Consequently, the synthesis of BiOCl using chlorine-containing IWS is a viable approach and can serve as a strategy for IWS valorization. This method also contributes valuable insights for the development of innovative synthesis techniques for BiOCl.

ACKNOWLEDGMENTS

This work was supported by the National Natural Science Foundation of China [22008185]; Shaanxi Province Science and Technology Plan Project[2024SF-YBXM-595]; Xi'an Science and Technology Plan Project [23GXFW0019].

REFERENCES

1. Wang H, Liu W, Haider MR, Ju F, Yu Z, Shi Y, Cai W, Wang A. Waste activated sludge lysate treatment: resource recovery and refractory organics degradation. J Hazard Mater. 2021;416:126206. https://doi.org/10.1016/j.jhazmat.2021.126206.
2. Liang Z, Yang W, Yin Z, Wang X, He Y, Yang K, Ma J. Chlor-alkali membrane cell process for industrial waste salt utilization:fundamentals and challenges. Desalination. 2024;587:117921. https://doi.org/10.1016/j.desal.2024.117921.
3. Shi J, Huang W, Han H, Xu C. Review on treatment technology of salt wastewater in coal chemical industry of China. Desalination. 2020;493:114640. https://doi.org/10.1016/j.desal.2020.114640.
4. Pisarska B, Jaroszek H, Mikołajczak W, Nowak M, Cichy B, Stopa H, Markowicz P. Application of electro-electrodialysis for processing of sodium sulphate waste solutions containing organic compounds: preliminary study. J Clean Prod. 2017;142:3741–3747. https://doi.org/10.1016/j.jclepro.2016.10.092.
5. Xi S, Wei X, Ding J, Wang W, Lu J. The removal of organic contaminants from industrial waste salts by pyrolysis and potential use for energy storage. J Clean Prod. 2023;425:138931. https://doi.org/10.1016/j.jclepro.2023.138931.
6. Chen X, Xing L, Zhou J, Wang K, Lu J, Han X. Spatial and temporal evolution and driving factors of county solid waste harmless disposal capacity in China. Front Environ Sci. 2023;10:1056054. https://doi.org/10.3389/fenvs.2022.1056054.
7. Xian L, Chen L, Tian H, Tao W-Q. Enhanced thermal energy storage performance of molten salt for the next generation concentrated solar power plants by SiO_2 nanoparticles: A molecular dynamics study. Appl Energy. 2022;323:119555. https://doi.org/10.1016/j.apenergy.2022.119555.
8. Yao K, Jia M, Wu H, Li Y, Chen C, Huang Y. Synthesis of BiOCl using Cl source from industrial wastewater and its application for wastewater treatment. Environ Technol. 2019;40(3):374–385. https://doi.org/10.1080/09593330.2017.1393014.
9. Li H, Zhang L. Photocatalytic performance of different exposed crystal facets of BiOCl. Curr Opin Green Sustain Chem. 2017;6:48–56. https://doi.org/10.1016/j.cogsc.2017.05.005.
10. Xie K, Xu S, Xu K, Hao W, Wang J, Wei Z. BiOCl Heterojunction photocatalyst: Construction, photocatalytic performance, and applications. Chemosphere. 2023;317:137823. https://doi.org/10.1016/j.chemosphere.2023.137823.
11. Wang Q, Miao Z, Zhang Y, Yan T, Meng L, Wang X. Photocatalytic reduction of CO_2 with H_2O mediated by Ce-tailored bismuth oxybromide surface frustrated lewis pairs. ACS Catal. 2022;12(7):4016–4025. https://doi.org/10.1021/acscatal.1c05553.
12. Dong X, Cui Z, Shi X, Yan P, Wang Z, Co AC, Dong F. Insights into dynamic surface bromide sites in $Bi_4O_5Br_2$ for sustainable N_2 photofixation. Angew Chem Int Ed. 2022;61(19):e202200937. https://doi.org/10.1002/anie.202200937.
13. Ouyang W, Teng F, Fang X. High performance BiOCl nanosheets/TiO_2 nanotube arrays heterojunction UV photodetector: the influences of self-induced inner electric fields in the BiOCl nanosheets. Adv Funct Mater. 2018;28(16):1707178. https://doi.org/10.1002/adfm.201707178.
14. Li K, Liang Y, Yang J, Gao Q, Zhu Y, Liu S, Xu R, Wu X. Controllable synthesis of {001} facet dependent foursquare BiOCl nanosheets: A high efficiency photocatalyst for degradation of methyl orange. J Alloys Compd. 2017;695:238–249. https://doi.org/10.1016/j.jallcom.2016.10.204.
15. Li Y, Wang X, Gao L. Construction of binary $BiVO_4$/g-C_3N_4 photocatalyst and their photocatalytic performance for reactive blue 19 reduction from aqueous solution coupling with H_2O_2. J Mater Sci Mater Electron. 2019;30(17):16015–16029. https://doi.org/10.1007/s10854-019-01972-z.
16. Hu Q, Di J, Wang B, Ji M, Chen Y, Xia J, Li H, Zhao Y. In-situ preparation of NH_2-MIL-125(Ti)/BiOCl composite with accelerating charge carriers for boosting visible light photocatalytic activity. Appl Surf Sci. 2019;466:525–534. https://doi.org/10.1016/j.apsusc.2018.10.020.
17. Cai M, Liu Y, Dong K, Wang C, Li S. A novel S-scheme heterojunction of $Cd_{0.5}Zn_{0.5}S$/BiOCl with oxygen defects for antibiotic norfloxacin photodegradation: Performance, mechanism, and intermediates toxicity evaluation. J Colloid Interface Sci. 2023;629:276–286. https://doi.org/10.1016/j.jcis.2022.08.136.
18. Wei W, Zuo H, Luo Y, Yang C, Chen H, He L, Lin H, Chen G, Luo W, Zeng B, et al. Broad spectral photodetectors based on BiOCl@boronate polymer core-shell heterojunctions. Chem Eng J. 2023;470:144198. https://doi.org/10.1016/j.cej.2023.144198.
19. Abdelrahman AA, El Naggar AMA, Morshedy AS. Production of an environmental friendly ultra-low sulfur diesel fuel under the effect of visible light irradiation using new nanocomposite based on $BiFeO_3$/BiOCl. Mater Chem Phys. 2023;307:128069. https://doi.org/10.1016/j.matchemphys.2023.128069.
20. Singh A, Giannakoudakis D, Arkas M, Triantafyllidis K, Nair V. Composites of lignin-based biochar with BiOCl for photocatalytic water treatment: RSM studies for process optimization. Nanomaterials (Basel). 2023;13(4):735. https://doi.org/10.3390/nano13040735.
21. Jiang J, Zhao K, Xiao X, Zhang L. Synthesis and facet-dependent photoreactivity of BiOCl single-crystalline nanosheets. J Am Chem Soc. 2012;134(10):4473–4476. https://doi.org/10.1021/ja210484t.
22. Li H, Shang J, Zhu H, Yang Z, Ai Z, Zhang L. Oxygen vacancy structure associated photocatalytic water oxidation of BiOCl. ACS Catal. 2016;6(12):8276–8285. https://doi.org/10.1021/acscatal.6b02613.
23. Dong F, Xiong T, Yan S, Wang H, Sun Y, Zhang Y, Huang H, Wu Z. Facets and defects cooperatively promote visible light plasmonic photocatalysis with Bi nanowires@BiOCl nanosheets. J Catal. 2016;344:401–410. https://doi.org/10.1016/j.jcat.2016.10.005.
24. Weng S, Pei Z, Zheng Z, Hu J, Liu P. Exciton-free, nonsensitized degradation of 2-naphthol by facet-dependent BiOCl under visible light: novel evidence of surface-state photocatalysis. ACS Appl Mater Interfaces. 2013;5(23):12380–12386. https://doi.org/10.1021/am403214r.
25. Hou W, Deng C, Xu H, Li D, Zou Z, Xia H, Xia D. n–p BiOCl@g-C_3N_4 heterostructure with rich-oxygen vacancies for photodegradation of carbamazepine. ChemistrySelect. 2020;5(9):2767–2777. https://doi.org/10.1002/slct.202000171.
26. Lin X, Xu D, Xi Y, Zhao R, Zhao L, Song M, Zhai H, Che G, Chang L. Construction of leaf-like g-C_3N_4/Ag/$BiVO_4$ nanoheterostructures with enhanced photocatalysis performance under visible-light irradiation. Colloids Surf A Physicochem Eng Asp. 2017;513:117–124. https://doi.org/10.1016/j.colsurfa.2016.11.040.
27. Che H, Liu C, Hu W, Hu H, Li J, Dou J, Shi W, Li C, Dong H. NGQD active sites as effective collectors of charge carriers for improving the photocatalytic performance of Z-scheme g-C_3N_4/Bi_2WO_6 heterojunctions. Catal Sci Technol. 2018;8(2):622–631. https://doi.org/10.1039/C7CY01709J.
28. Wang C, Zhang A, Peng D, Mei Y, Wang Y, Guo J, Tan Z, Liu Y, Li H. Facile fabrication of 3D spherical Ag_2WO_4 doped BiOI/BiOCl double S-scheme heterojunction photocatalyst with efficient activity for mercury removal. J Environ Chem Eng. 2022;10(6):108517. https://doi.org/10.1016/j.jece.2022.108517.
29. Yang P, Su X, Huang S, Zhong J, Li M. Juncus effuses biochar-assisted preparation of oxygen vacancies-rich BiOCl for photocatalytic degradation of pollutants and CO_2 reduction. Mater Today Commun. 2024;41:110564. https://doi.org/10.1016/j.mtcomm.2024.110564.
30. Li H, Li J, Ai Z, Jia F, Zhang L. Oxygen vacancy-mediated photocatalysis of BiOCl: reactivity, selectivity, and perspectives. Angew Chem Int Ed. 2018;57(1):122–138. https://doi.org/10.1002/anie.201705628.
31. Li H, Shi J, Zhao K, Zhang L. Sustainable molecular oxygen activation with oxygen vacancies on the {001} facets of BiOCl nanosheets under solar light. Nanoscale. 2014;6(23):14168–14173. https://doi.org/10.1039/C4NR04810E.
32. Ye L, Zan L, Tian L, Peng T, Zhang J. The {001} facets-dependent high photoactivity of BiOCl nanosheets. Chem Commun (Camb). 2011;47(24):6951. https://doi.org/10.1039/c1cc11015b.
33. Zhao K, Zhang L, Wang J, Li Q, He W, Yin JJ. Surface structure-dependent molecular oxygen activation of BiOCl single-crystalline nanosheets. J Am Chem Soc. 2013;135(42):15750–15753. https://doi.org/10.1021/ja4092903.
34. Li M, Zhang Y, Li X, Yu S, Du X, Guo Y, Huang H. In-depth insight into facet-dependent charge movement behaviors and photo-redox catalysis: A case of {001} and {010} facets BiOCl. J Colloid Interface Sci. 2017;508:174–183. https://doi.org/10.1016/j.jcis.2017.08.042.
35. Wang Q, Wang W, Zhong L, Liu D, Cao X, Cui F. Oxygen vacancy-rich 2D/2D BiOCl-g-C_3N_4 ultrathin heterostructure nanosheets for enhanced visible-light-driven photocatalytic activity in environmental remediation. Appl Catal B. 2018;220:290–302. https://doi.org/10.1016/j.apcatb.2017.08.049.

36. Li X, Sun S, Zhang X, Zhang X, Cui J, Yang Q, Liang S. Three-in-one to enhance visible-light driven photocatalytic activity of BiOCl: synergistic effect of mesocrystalline stacking superstructure, porous nanosheet and oxygen vacancy. J Materiomics. 2021;7(2):328–338. https://doi.org/10.1016/j.jmat.2020.10.012.
37. Li H, Zhang L. Oxygen vacancy induced selective silver deposition on the {001} facets of BiOCl single-crystalline nanosheets for enhanced Cr(vi) and sodium pentachlorophenate removal under visible light. Nanoscale. 2014;6(14):7805–7810. https://doi.org/10.1039/C4NR01315H.
38. Wang S, Song D, Liao L, Li M, Li Z, Zhou W. Surface and interface engineering of BiOCl nanomaterials and their photocatalytic applications. Adv Colloid Interface Sci. 2024;324:103088. https://doi.org/10.1016/j.cis.2024.103088.
39. Li H, Shang J, Ai Z, Zhang L. Efficient visible light nitrogen fixation with BiOBr nanosheets of oxygen vacancies on the exposed {001} facets. J Am Chem Soc. 2015;137(19):6393–6399. https://doi.org/10.1021/jacs.5b03105.
40. Shan L, He L, Suriyaprakash J, Yang L. Photoelectrochemical (PEC) water splitting of BiOI{001} nanosheets synthesized by a simple chemical transformation. J Alloys Compd. 2016;665:158–164. https://doi.org/10.1016/j.jallcom.2016.01.008.
41. Xiong J, Cheng G, Li G, Qin F, Chen R. Well-crystallized square-like 2D BiOCl nanoplates: mannitol-assisted hydrothermal synthesis and improved visible-light-driven photocatalytic performance. RSC Adv. 2011;1(8):1542–1553. https://doi.org/10.1039/c1ra00335f.